Enhanced MOIDS-derived ice physical properties within CoLM revealing bare ice-snow-albedo feedback over Greenland

Shuyang Guo[1], Yongjiu Dai[1]*, Hua Yuan[1], Hongbin Liang[1]

[1] Southern Marine Science and Engineering Guangdong Laboratory (Zhuhai), School of Atmospheric Science, Sun Yat-sen University, Zhuhai, China

Corresponding author: Yongjiu Dai (daiyj6@mail.sysu.edu.cn)

Submitted to *The Cryosphere*

Abstract

Under global warming, the Greenland Ice Sheet (GrIS) is experiencing unprecedented mass loss. One key contributing factor is the change in snow and ice albedo, which is closely related to firn metamorphism. To investigate the impact of bare ice microstructure changes on the regional warming of the GrIS ablation zone, SNICAR-ADv4 (Snow, Ice and Aerosol Radiation model Adding-Doubling Version 4), a physically based radiative transfer model, is incorporated in Common Land Model version 2024 (CoLM2024). It allows the land surface model represent the ice albedo with changes in ice properties rather than using a constant ice albedo value. Quality control was conducted on the bare ice physical property dataset input into CoLM, with multiple MODIS products combined to ensure accuracy. The application of SNICAR-ADv4 reduced the overestimation of shortwave broadband albedo by 38%, with a bias of only 0.053. Further sensitivity experiments indicate that the summer albedo in the bare ice region is reduced by 0.032 due to the bare ice metamorphism, producing a 2-m temperature forcing of 0.071°C, a snow cover change of -0.011, and a snow water equivalent forcing of -1.345 mm. These changes lead to increased bare ice exposure, further reducing albedo and enhancing solar radiation absorption by the surface, thereby reinforcing a feedback involving bare ice, snow, and albedo. This highlights the critical role of bare ice physical properties in amplifying melt through the bare ice-snow-albedo feedback, with stronger feedbacks expected under a fully coupled land-atmosphere model.

删除[o_0]: Meanwhile, q

删除[o_0]: 60

删除[o_0]: during the summer

删除[o_0]: and a snow cover change of -0.011

Keywords

Greenland Ice Sheet; Bare ice region; Ice albedo; Albedo feedback; MODIS; Remote sensing

1. Introduction

The Greenland Ice Sheet (GrIS), the last remnant of the Ice Age has been melting at a rapid pace since the 1990s, losing around 255 Gt of ice annually in 2003-2016 (Sasgen et al., 2020; Li et al., 2022; van den Broeke et al., 2017). The negative mass balance of the GrIS and

peripheral glaciers is the most significant cryospheric factor driving sea level rise, contributing over 25% of observed global sea level rise (Chen et al., 2017; Ryan et al., 2019). Such melting was linked to a combination of processes including climate warming, reduced retention capacity of firn and lower surface albedo (Hofer et al., 2017; King et al., 2020; Ryan et al., 2024). The total mass loss from GrIS consists of two components: surface runoff and frontal ablation occurring at the terminus of outlet glaciers (Cogley et al., 2011, Kochtitzky et al., 2023). Surface losses have exceeded frontal losses in contributing to GrIS mass loss since 2000, with 55% of Greenland's total mass loss attributed to surface mass balance and 45% to the discharge of outlet glaciers between 2000-2018 (Mouginot et al., 2019).

Ice discharge on the surface of the GrIS is partially regulated by the surface albedo. It serves as a fundamental parameter in controlling the absorption of insolation by the ice sheet (Box et al., 2012; Naegeli et al., 2017, Feng et al., 2024). A minor change in snow and ice surface albedo can exert a substantial effect on the energy budget of regional surface-air system, causing significant fluctuations in the energy flux on the surface of the GrIS (Nolin and Stroeve, 1997). Surfaces with high albedo, such as fresh snow, efficiently reflect solar radiation, whereas darker areas, such as glacier ice, absorb the majority of incoming shortwave energy (Whicker-Clarke et al., 2022). Snow and ice albedo varies with the spatial distribution of snow, ice, and biotic and abiotic light absorbing constituents (LACs) and further evolves with the melting of snowpack and glacier surfaces through the spring and summer. Fluctuations in the snowline dictate the relative extent of dark bare ice versus brighter snow (Ryan et al., 2019). These directly influence GrIS surface melt through the exposure of bare ice (Antwerpen et al., 2022) and the processes that darken bare ice itself (Chevrollier et al., 2023). Dark bare ice extent closely tracks interannual variations in snowline elevation and is exposed as the snowline retreats further inland during the melt season, leading to the reduction of ice sheet albedo and the intensified melt. This positive feedback has been referred to as the "snow-albedo feedback" (Ryan et al., 2019).

In the preceding decades, polar amplification has contributed to the progressive darkening of

删除[o_0]: Whicker

删除[o_0]:

删除[o_0]: Fluctuations in the snowline dictate the relative extend of dark bare ice and brighter snow (Ryan et al., 2019), and GrIS's surface melt can be attributed to the exposure of bare ice (Antwerpen et al., 2022) and the processes that darken bare ice itself (Chevrollier et al., 2023).

删除[o_0]: was

the GrIS and the prolongation of the melt season, both of which serve as positive feedback mechanisms that intensify surface melt (Tedesco et al., 2016). As the warming occurs over the ice surface, bare ice albedo is reduced through melt processes that darken the ice surface. Notably, these processes include exposure of dust layers, pooling of surface meltwater, increased interstitial water content, and liquid meltwater-induced growth of pigmented ice algal assemblages that inhabit the bare ice surface (Cook et al., 2020; Stibal et al., 2017; Tedstone et al., 2020; Williamson et al., 2018; Whicker-Clarke et al., 2022). Despite operating over a relatively small area of the ice sheet, it is argued that these bare ice processes have contributed substantially to an observed reduction in albedo and associated increase in melt across GrIS's ablation zone from 2000 to 2011 (Stibal et al., 2017; Tedstone et al., 2017). This category of physical and biological melt-albedo processes that darken bare ice is referred as the "bare ice-albedo feedback" (Ryan et al., 2019). However, the complex and non-linear response of regional snow and ice, particularly in ablation zones, to changes in meteorology and climate highlights the growing necessity to model these surfaces using physical principles rather than relying solely on empirical methods (Box et al., 2012). Therefore, accurately modeling the influence of snow and ice on the albedo of the GrIS becomes increasingly important to capture these dynamics effectively.

删除[o_0]: in

删除[o_0]: Whicker

The albedo of the cryosphere varies widely depending on the solar zenith angle (SZA), atmospheric conditions, metamorphic state of the snow and ice, and impurities (He and Flanner, 2020). The Snow, Ice, and Aerosol Radiative (SNICAR) model is one of the most widely used snowpack radiative transfer models (Flanner et al., 2021). Initially, it combined the theory from Wiscombe and Warren (1980) and Warren and Wiscombe (1980) with the multi-layer two-stream solution from Toon et al. (1989) to enhance the simulation of snow albedo (Flanner et al., 2007). Updates and new features have also been incorporated within SNICAR, including eight species of LACs (Flanner et al., 2007), four snow grain shapes (He et al., 2018), black carbon-snow and dust-snow internal mixing state (Flanner et al., 2012; He et al., 2017, 2019). Dang et al. (2019) developed SNICAR-AD by substituting the tri-diagonal matrix solution solving method (Toon et al., 1989) with the delta-Eddington adding-doubling radiative method, as a result of the latter's superior computational stability

across varying solar zenith angles and higher computational efficiency (He et al., 2024). To represent ice albedo, Whicker-Clarke et al. (2022) further developed SNICAR-ADv4 by integrating and extending key features from earlier radiative transfer models to achieve more accurate simulations of a spectrally resolved cryospheric column of snow and ice with a refractive boundary, while incorporating light-absorbing constituents (LACs), such as black carbon (BC) and algae, into this standalone radiative transfer model. It simulates bare ice using the physical microscopic structure of the ice, including the ice density, the scattering air bubbles within an absorbing ice medium, and a refractive boundary that depicts the refraction across snow-ice interfaces (Briegleb and Light, 2007; Gardner and Sharp, 2010; Mullen and Warren, 1988).

Nevertheless, the ice albedo is typically prescribed as a constant value in the visible (VIS) and near-infrared (NIR) spectral regions in Earth system models (ESMs). For instance, Ice albedo is 0.6 in the visible and 0.4 in the NIR in the default version of the Energy Exascale Earth System Model (E3SM) and the Community Earth System Model (CESM) version 2 (Whicker-Clarke et al., 2024). Such parameterization does not capture the albedo of solid ice or variations in spectral albedo with changing ice conditions. To advance ice radiative transfer modeling in Earth system models (ESMs), Whicker-Clarke et al. (2024) incorporated SNICAR-ADv4 into the E3SM, in which the GrIS ice physical properties are retrieved by the satellite observation data. This enhancement enables more realistic simulations of the GrIS bare ice albedo, and concurrently reveals that the default ELM method overestimates bare ice albedo by 4% in the visible and 7% in the NIR bands. However, the quality information of MODIS albedo products were not considered in the process of acquiring bare ice properties in their study. Schaaf et al. (2011) noted that the MODIS poor-quality inversions beyond a SZA of 70° are characterized by high noise and often significantly lower than the more stable and consistent values observed at smaller SZAs. Omitting quality flags could, therefore, lead to an underestimation of Greenland's snow/ice albedo and introduce significant uncertainties in the retrieval of bare ice physical properties. Despite the aforementioned modeling advances, the Common Land Model (CoLM) still uses fixed values to represent ice albedo (0.60 in the visible and 0.40 in the NIR). For the purpose of investigating the impacts of bare

删除[o_0]: Whicker
删除[o_0]: offline
删除[o_0]: Whicker
删除[o_0]: Whicker
删除[o_0]: 80
删除[o_0]: 55

ice metamorphism under polar warming, it is also imperative to incorporate ice radiative transfer techniques into CoLM to enhance albedo modeling with more realistic and physical representations of snow-ice-LAC-radiation interactions.

In this study, we focus on the bare ice region of the GrIS, characterized by the presence of land ice, and bare ice is exposed with snow melting during ablation season. The aim of this study is to develop a more reliable dataset of Greenland's bare ice physical properties by incorporating the quality information of MODIS albedo products, and explore the bare ice-albedo feedback associated with the metamorphism of bare ice after the implementation of the SNICAR-ADv4 into the CoLM. This paper is organized as follows. Section 2 provides descriptions of the CoLM snow and ice albedo schemes and details the model simulations, as well as the explanation of the use of various MODIS products to inform the ice albedo calculations in SNICAR-ADv4. Section 3 compares the differences in albedo simulations with and without ice radiative transfer solver (SNICAR-AD and SNICAR-ADv4), and quantified the impact of varying bare ice properties on the near-surface air temperature and the snow cover. Section 4 is conclusions and discussion.

删除[o_0]: in

删除[o_0]: y

2. Models, Data, and Methods

2.1 Snow and Ice Albedo Scheme

删除[o_0]: **CoLM**

This study utilizes two distinct implementations of the SNICAR model within the CoLM for snow and ice albedo simulations: (i) the baseline SNICAR-AD version (Dang et al., 2019) and (ii) the enhanced SNICAR-ADv4 version (Whicker-Clarke et al., 2024). Both versions adopt identical snow albedo algorithms but exhibit distinct ice albedo treatments. Specifically, as shown in Figs. 1a and b, the SNICAR-ADv4 accounts for radiative transfer through the ice column, while the SNICAR-AD prescribes ice albedo as constant values: 0.6 for visible (VIS: 0.3–0.7 μm) and 0.4 for near-infrared (NIR: 0.7–5.0 μm) bands. The snow albedo scheme of SNICAR-AD/SNICAR-ADv4 in the CoLM computes snow albedo for the multi-layer (up to 5 layers) snowpack with the two stream radiative transfer scheme of the delta-Eddington

approximation and adding-doubling technique, accounting for the effects of snow properties (e.g., size and shape) and LAC contamination on snow albedo.

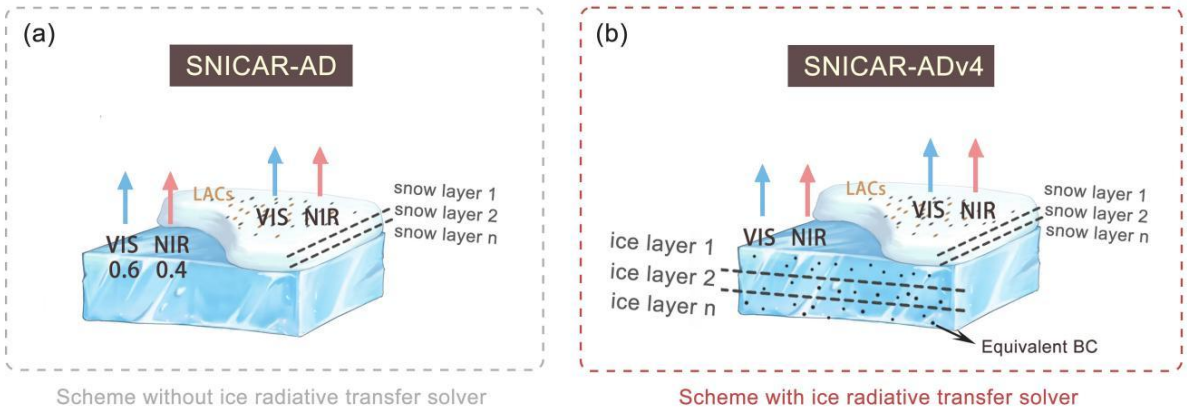

Figure 1. Schematic representation of the snow and land ice column in CoLM SNICAR-AD and SNICAR-ADv4.

For snow albedo simulation, the SNICAR-AD/SNIACR-ADv4 embedded in CoLM uses the physical properties of the snowpack and albedo of the top layer of the underlying ground to determine the column albedo (Flanner and Zender, 2006). The input variables consist of direct and diffuse radiation, the surface downward solar spectrum, the solar zenith angle (for direct radiation), the ground albedo beneath the snowpack, vertical profiles of snow grain size, snow layer thickness and density, aerosol concentrations of each snow layer, as well as the optical properties of both snow and aerosols. Meanwhile, parameterizations for snow grain shapes (sphere, spheroid, hexagonal plate, and Koch snowflake) and LACs-snow mixing states (BC/dust externally or internally mixed with snow grains) are included to improve the simulations of snow surface energy and water balances (Hao et al., 2023).

For ice albedo modeling, the advent of the SNICAR-ADv4 enables us to explore the regional climatic response induced by changes in ice albedo using the ice microphysical properties derived from satellite products. As proposed by Whicker-Clarke et al. (2024), the radiation transfer process within the ice layer can be calculated in the land surface model, which requires input variables such as ice density, air bubble effective radii within the ice, equivalent BC concentrations, and downward solar spectra. The need for air bubble

parameters arises from the representation of ice layers as collections of independently scattering air bubbles within a solid ice medium in SNICAR-ADv4, while snow layers are treated as independently scattering ice crystals in an air medium (Picard et al., 2016; Whicker-Clarke et al., 2022).

2.2 Data

MODIS MCD12C1, MOD09CMG, and MOD10C1 products with consistent 0.05° spatial resolution were utilized for GrIS bare ice monitoring during the summer melt seasons of 2000-2020. The MCD12C1 Version 6.1 annual land cover type product (Friedl et al., 2010) provided initial cryospheric classification by excluding grids not categorized as snow or ice. The MOD09CMG (Vermote 2021) band 2 reflectance (0.841–0.876 μm) was employed for bare ice-snow discrimination, where pixels with reflectance values below 0.6 were classified as bare ice. Comparative spectral analysis of MODIS imagery by Shimada et al. (2016) revealed markedly greater surface reflectance in snow-covered pixels relative to bare ice across all spectral bands, with maximal contrast observed at 0.86 μm. The robustness of this threshold was confirmed by Antwerpen et al. (2022) through comparison with Landsat 8 OLI (Operational Land Imager), with a relative error of 0.16%. The MOD10C1 product was further used to exclude pixels with cloud obstruction percentage exceeding 90% or snow cover fraction above 90% (Antwerpen et al., 2022; Whicker-Clarke et al., 2024). The derived bare ice extent was filtered by excluding pixels above the mean equilibrium line altitude of 1679 m a.s.l., defined as the 95th percentile of ablation zone elevations. This conservative threshold minimizes sporadic high-elevation detections while maintaining robust estimation of the mean equilibrium line altitude (Antwerpen et al., 2022).

The MODIS MCD43C3 product (Schaaf et al., 2002) is used to retrieve bare ice physical properties by using standalone SNICAR-ADv4 and evaluate CoLM-simulated albedo over the GrIS bare ice regions. This daily product provides spectral (MODIS bands 1 to 7) and broadband (VIS 0.3–0.7 μm, NIR 0.7–5.0 μm and shortwave 0.3–5.0 μm) black-sky albedo (BSA) and white-sky albedo (WSA) at local solar noon, derived from 16 days of Aqua-Terra merged surface albedo dataset based on the bidirectional reflectance distribution function

(BRDF) algorithm (Schaaf and Wang, 2021). Among the GLASS-AVHRR and C3S-v2 albedo products, MCD43C3 stands out as the most reliable for monitoring snow albedo, exhibiting the lowest bias and RMSE over snow and consistent performance across diverse snow cover conditions (Urraca et al., 2022). In the GrIS, MCD43A3 was found to outperform the GLASS albedo product and even the reconstructed albedo based on the MOD10A1, for the sites located in the GrIS ablation zone (Ye et al., 2023).

Considering the little difference between BSA and WSA for a typical summer day, using BSA is considered acceptable for analyzing the GrIS during the summer (Alexander et al., 2014; Stroeve et al., 2005). The extracted variables in this study from MODIS MCD43C3 include Band 2 BSA, broadband BSA (visible, near-infrared and shortwave), along with local noon solar zenith angles (SZAs) and albedo quality index. The MCD43C3 albedo quality index helps identify regions with cloud cover contamination, detrimental atmospheric conditions, or insufficient observational data. Figure 2a shows the daily variation of the regionally weighted average SZA over Greenland during May-September. The period with SZA>70° occurs primarily in September. For the relationship between the SZAs of MCD43C3 and their spatiotemporally corresponding albedo quality index (Fig. 2b), it can be seen that the percentage of low-quality indices (4 and 5) rises drastically as the SZA increases at higher SZA. Therefore, we excluded albedo values identified with a low-quality index when the SZA exceeded 70° to derive more reliable satellite-retrieved bare ice physical properties.

设置格式[o_0]: 字体: 非加粗

设置格式[o_0]: 字体: 非加粗

设置格式[o_0]: 字体: 非加粗

设置格式[o_0]: 字体: 非加粗

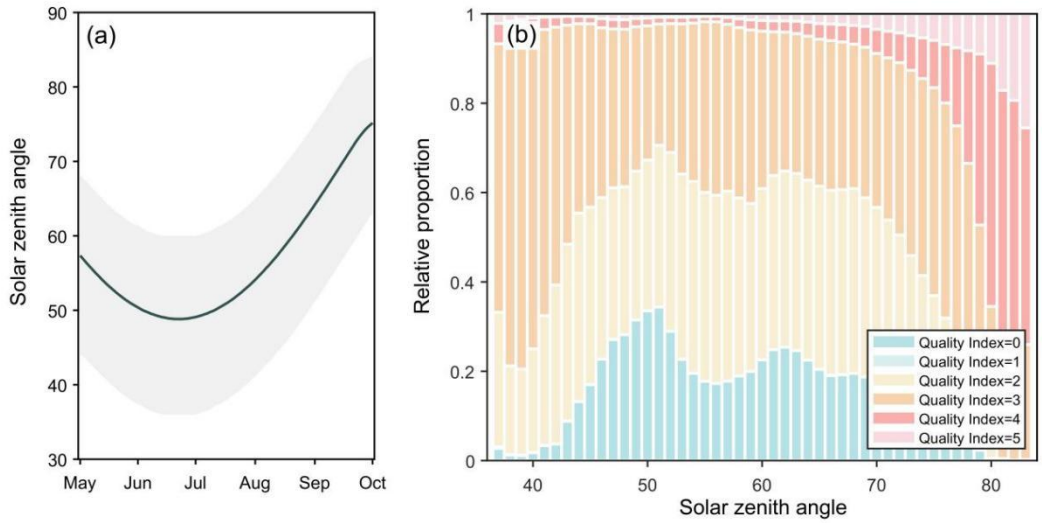

Figure 2. Regional-weighted mean SZAs of Greenland at local noon from May to September (a; solid line). Grey shaded area represents the range of SZAs over Greenland. Relative proportion of the quality index of MCD43C3 albedo dataset under different SZAs over Greenland during May to September (b; 0 for best quality and 5 for poorest quality)

2.3 Method

The method for obtaining ice physical properties (ice density, air bubble effective radius and equivalent BC) from MODIS bare ice albedo involves two main steps (Whicker-Clarke et al., 2024). First, as detailed in Section 2.2, bare ice spatiotemporal distribution was determined through the integrated use of MODIS products, employing MCD12C1 to exclude non-cryospheric pixels, MOD09CMG to distinguish bare ice from snow cover, and MOD10C1 to apply snow and cloud masking. Second, the bare ice physical properties (ice density and air bubble effective radius) are retrieved using MCD43A3 band 2 BSA and its corresponding SZA to match the closest physical properties within the precomputed lookup table by standalone SNICAR-ADv4 model. Notably, this step derives only ice density and air bubble effective radius, whereas equivalent black carbon (BC) concentration requires additional processing steps described later in this section. After obtaining all bare ice physical properties (ice density, air bubble effective radius, and equivalent BC concentration), we upscaled the data from a spatial resolution of 0.05°×0.05° to 0.5°×0.5°.

The lookup table was generated using the standalone SNICAR-ADv4 radiative transfer model by testing a range of parameter combinations within physically constrained ranges, including ice density (650-916 kg·m^{-3}) and air bubble radii (100-1500 μm), as well as the SZAs spanning 35° to 75° to represent typical local noon conditions across the GrIS grid cells. Ice with densities above 650 kg·m^{-3} is conventionally classified as cryospheric media, consistent with in situ measurements (Whicker-Clarke et al., 2022). However, because the density-bubble radius relationship for GrIS bare ice remains poorly constrained, we apply a linear density-radius relationship as a first-order approximation for calculating the specific surface area (SSA), where densities of 650 kg·m^{-3} and 916 kg·m^{-3} corresponding to bubble radii of 50 μm and 1500 μm, respectively (Fig. 3a). This parameterization is provisional and awaits future observational validation. For each parameter combination, the band 2 albedo, SSA and the volume fraction of air (V_{air}) were then output by the standalone SNICAR-ADv4. The SSA is a measure of the total surface area of ice-air interfaces relative to the ice mass. The relationship between the SSA (α, units: m^2·kg^{-1}) and ice density and air bubble effective radius is given by Eq.1, where ρ_{blk} is layer bulk ice density used to calculate the volume fraction of air (Eq.2).

设置格式[o_0]: 上标

$$\alpha = \frac{3V_{air}}{\rho_{blk} R_{eff}} \quad \text{(Eq. 1)}$$

$$V_{air} = \frac{\rho_{ice} - \rho_{blk}}{\rho_{ice}} \quad \text{(Eq. 2)}$$

Figure 3b shows the band 2 albedo from the SNICAR-ADv4 lookup table as a function of SSA. This functional degeneracy indicates that the radiative transfer modeling depends primarily on the SSA rather than the specific ice density/bubble size combination. Consequently, the retrieval algorithm selects the (density, radius) combination that most closely reproduces the observed Band 2 albedo. Since MCD43C3 provides the band 2 albedo and SZA for each bare ice grid cell, the corresponding bare ice physical properties can be inferred from the lookup table. It is important to note, however, the resulting bare ice property maps (Figs. 3c-f) represent just one plausible solution among several combinations that could yield similar SSA and albedo values.

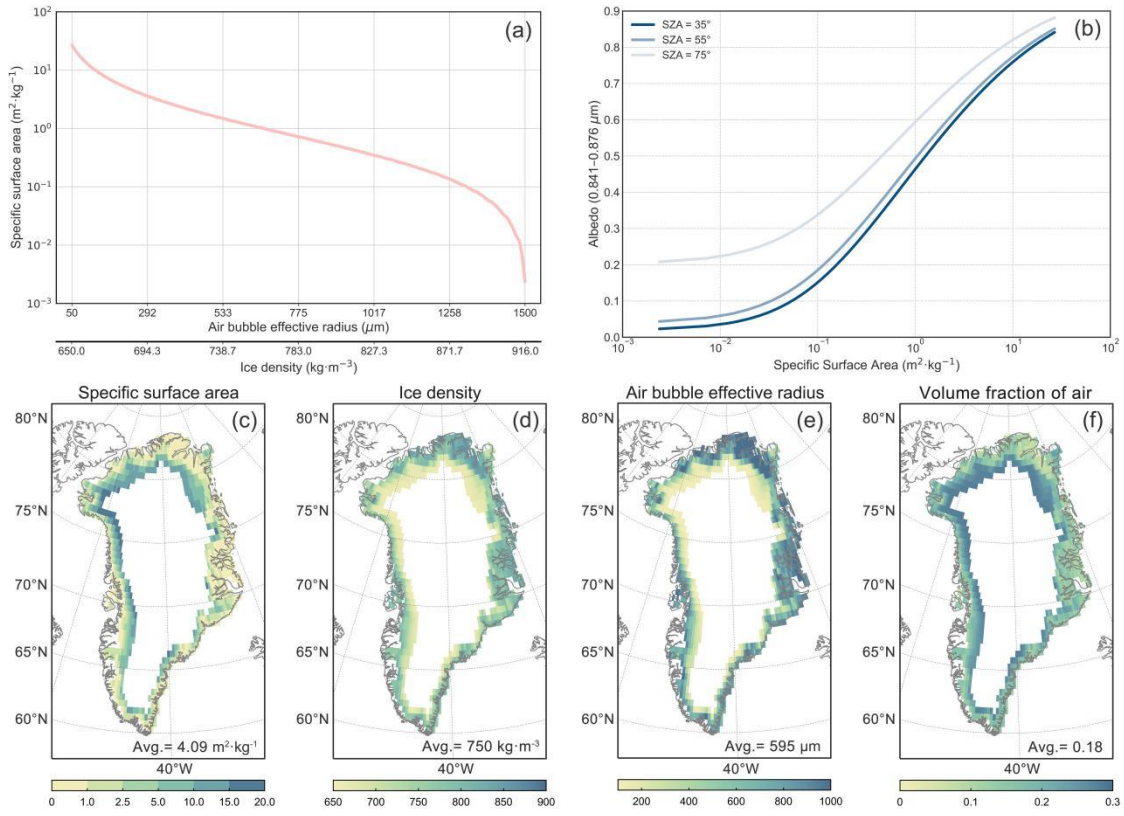

Figure 3. The relationship between ice specific surface area (SSA; $m^2 \cdot kg^{-1}$), air bubble effective radius (μm) and ice density ($kg \cdot m^{-3}$) under a linear density-radius relationship (a first-order approximation) assumed in this study (a). MCD43C3 band 2 (0.841-0.876 μm) albedo as a function of SSA and solar zenith angle (b). Spatial distribution of JJA (c) specific surface area ($m^2 \cdot kg^{-1}$), (d) ice density ($kg \cdot m^{-3}$), (e) air bubble effective radius (μm) and (f) volume fraction of air in the period of 2000-2020.

After acquisition of the daily ice density and air bubble effective radius of the GrIS (Figs. R3d and 2e), we again employed the standalone SNICAR-ADv4 model to simulate the NIR and visible albedo for each bare ice grid cell of the GrIS. Using an iterative optimization approach, we derived the equivalent BC concentration by adjusting the BC input parameter in the standalone SNICAR-ADv4 until its simulated visible albedo matched the MODIS MCD43C3 observations. This inversion method relies on the strong influence of LACs on visible albedo and their negligible impact on NIR albedo over bare ice (Schneider et al., 2019). As seen in Figs. 4a-c, there is minimal difference in the albedo in the NIR band, with a slight underestimation of 0.029 by the standalone SNICAR-ADv4. In contrast, the

297 SNICAR-ADv4 significantly overestimated the visible albedo by up to 0.293 when using
298 these bare ice properties, as it did not account for the LACs (Figs. 3d-f). We incrementally
299 adjusted the input BC concentration in the standalone SNICAR model to match the visible
300 albedo values from MCD43C3 data at each GrIS bare ice grid cell (Figs. 4h and i). This
301 process yielded the daily equivalent BC concentrations shown in Fig. 4g. Based on the
302 MODIS data and the standalone SNICAR-ADv4 lookup table, the daily 0.5-deg ice density,
303 air bubble effective radius and equivalent BC data were then processed into monthly
304 timescale as input for CoLM. Besides, it is worth mentioning that not all bare ice grid cells
305 are informed by the bare ice physical properties data in each summer month. These grid cells
306 are filled with the climatological mean values of bare ice physical properties when retrievals
307 fail due to clouds or poor data quality.

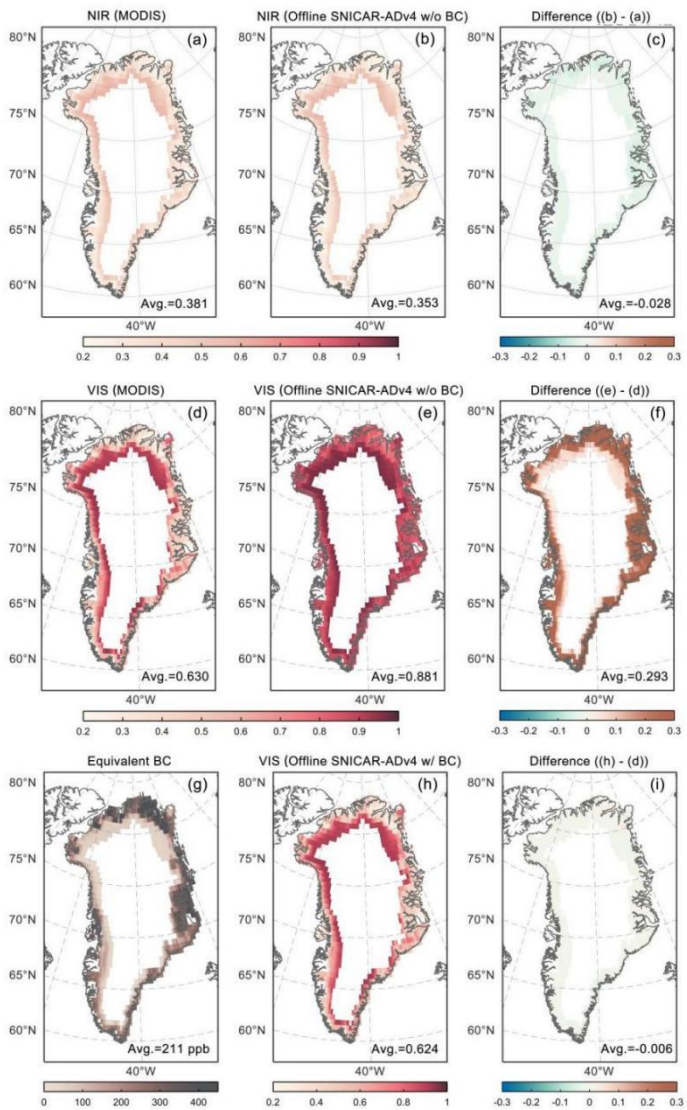

308

Figure 4. The spatial distributions of MODIS bare ice albedo and standalone SNICAR-ADv4 bare ice albedo excluding LACs in (a, b) near-infrared and (c, d) visible bands for the JJA from 2000 to 2020, along with (c, f) their differences. The spatial distributions of (g) equivalent black carbon, (h) the standalone SNICAR-ADv4 bare ice visible albedo with equivalent black carbon (ppb), and (i) its difference from the MODIS bare ice visible albedo.

We use the standalone SNICAR-ADv4 and briefly examine aforementioned factors influencing spectral albedo of ice with direct light conditions, including the SZA, ice density, air bubble effective radius (R_{eff}), and equivalent BC. As shown in Fig. 5a, total internal reflection occurs at wavelengths around 3μm for SZA greater than 55°, and the wavelength range for total internal reflection expands with the increases in SZAs. This phenomenon occurs for pure and smooth ice surfaces but is not representative of naturally occurring ice, which typically has impurities and rough surfaces. For the dependency of albedo on ice density, air bubble effective radius, the spectra show that the albedo declines as the ice density and air bubble radius increases since air bubbles within ice are responsible for the scattering light and smaller bubbles scatter light more efficiently in the visible and near-infrared parts of the spectrum (Figs. 5b-c). Furthermore, BC impacts ice albedo rather uniformly across the visible spectrum and has almost no impact at $\lambda > 1.0$ μm.

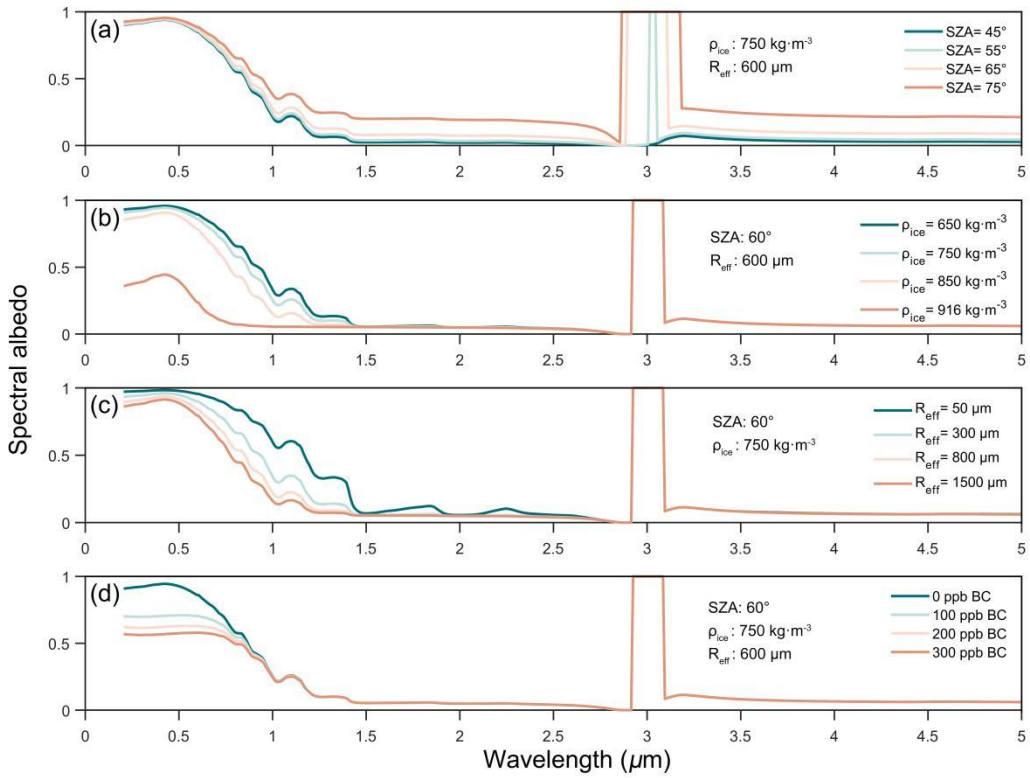

Figure 5. Spectral albedo simulated by standalone SNICAR-ADv4 under direct incident irradiance with varing (a) SZA, (b) ice density, (c) air bubble effective radius and (d) BC concentration.

2.4 Model simulation

删除[o_0]:

We conduct several offline CoLM simulations with the embedded SNICAR-ADv4 and SNICAR-AD schemes on a 0.5×0.5-degree resolution driven by the atmospheric forcing from the 6-hourly European Center for Medium-Range Weather Forecast's fifth-generation atmospheric Reanalysis (ERA5) in the GrIS. Compared with other atmospheric forcings, ERA5's precipitation rates exhibit a higher correlation with measured net accumulation over the GrIS (Schneider et al., 2023). We run the model simulations for the years 1980–2020 and the summer melt season (June, July and August; JJA) during 2000-2020 is used for analysis. Aerosol concentration in the snow layer is calculated based on the prescribed monthly aerosol (BC, dust, OC) wet and dry deposition flux from the CESM2-WACCM simulations participated in CMIP6 experiments (Danabasoglu et al., 2020). The monthly bare ice

删除[o_0]: land-only

properties for ice radiative transfer process are inferred from MODIS products using the standalone SNICAR-ADv4 over the bare ice region of the GrIS, covering the JJA from 2000 to 2020, as the MODIS products has been available since 2000. To prevent possible unusual model behavior when shifting bare ice albedo schemes, the bare ice properties from the summer of 2000 were used in a brief spin-up run for the variable bare ice conditions in our experimental runs from 1998 to 2000. For land ice patches informed by the ice properties, the bare ice albedo is first calculated and replaces the constant values (0.6 for VIS and 0.4 for NIR). If snow is present over the ice, the new ice albedo of underlying ice column is used as the lower boundary to calculate snow albedo. The total patch albedo is then determined by the fractional coverage of land types and snow cover.

删除[o_0]: 0.8

删除[o_0]: 0.55

In this study, we analyzed output variables from three sets of CoLM simulations: (1) those using SNICAR-AD with fixed bare ice albedo (0.6 for visible and 0.4 for near-infrared), (2) those using SNICAR-ADv4 with annually-varying bare ice properties and (3) those using SNICAR-ADv4 with bare ice properties held constant at year 2000 values for all years. The simulations output two variable groups: (a) surface albedo (visible, near-infrared, and shortwave under direct radiation) and bare ice fraction for albedo evaluation; (b) 2-m temperature, snow cover fraction, and snow water equivalent to quantify the effect from the bare ice metamorphism.

3. Results

3.1 Mapping of GrIS bare ice physical properties

Figures 3b-e display the spatial distribution of summer climatological mean of the bare ice physical properties, including SSA, ice density, air bubble effective radius and volume fraction of air. The bare ice density gradually decreases from the lower-elevation coastal regions toward the interior, while the volume fraction of air show an opposite pattern for it is calculated by bulk ice-air mixture density and pure ice density (Figs. 3c and e). SSA represent the total surface area of ice-air interfaces relative to the mass of ice, determined by the volume fraction of air, effective diameter of air bubbles, and the bulk density of the ice

删除[o_0]: 2

删除[o_0]: demonstrate

删除[o_0]: ure

删除[o_0]: 2

删除[o_0]: 2

layer (Whicker-Clarke et al., 2022), with high-value area distributed in the area along the mean equilibrium line (Fig. 3b). Given the large discrepancy in bare ice visible albedo between the standalone SNICAR-ADv4 without LACs and the MCD43C3 in the coastal regions of the GrIS (Figs. 4d and e), higher equivalent BC concentrations occur in these areas compared to inland regions, indicating potentially more severe contamination, particularly in the southeastern and northernmost parts of the GrIS (Fig. 3g).

3.2 Spatial and Temporal performance of CoLM Simulations

The bare ice region of the GrIS in this study is defined as grid cells with exposed glacier ice (snow cover fraction <100%), where surface albedo is controlled by ice properties but also influenced by residual snow and bare soil patches. Figure 6a shows the spatial distribution of land ice underlying the snowpack. The areas where land ice is the main type of land cover are located in the periphery of the the GrIS with the exception of the southeastern edge. Values of land ice fraction below 1 implies that the corresponding grid cells contain other land cover type, e.g. bare soil. The exposed bare ice fraction (Fig. 6b) is calculated accounting for the snow coverage in each grid cell, utilizing the SNICAR-AD scheme. It is important to note that, despite a slight difference in snow cover fraction simulations, the choice of snow albedo scheme does not affect the selection of bare ice regions. The exposed bare ice fraction frequency distribution is shown in Fig. 6c, in which the bare ice fraction spans from 0 to 0.7, and in most areas, the bare ice fraction is less than 0.5.

删除[o_0]: Whicker
删除[o_0]: ure
删除[o_0]: 2
删除[o_0]: offline
删除[o_0]: ure
删除[o_0]: 3
删除[o_0]: 3
删除[o_0]: there are higher concentrations of equivalent BC in these areas compared to those farther inland, indicating potentially more severe contamination, particularly in the southwest, east, and northernmost parts of the GrIS (Figure 3g)
删除[o_0]: means these grid cells may also contain
删除[o_0]: In tandem with the effect of snow cover simulated by SNICAR-ADv4 enabled CoLM, t
删除[o_0]: ure
删除[o_0]: 5
删除[o_0]: Figure
删除[o_0]: 3
删除[o_0]: d
删除[o_0]:

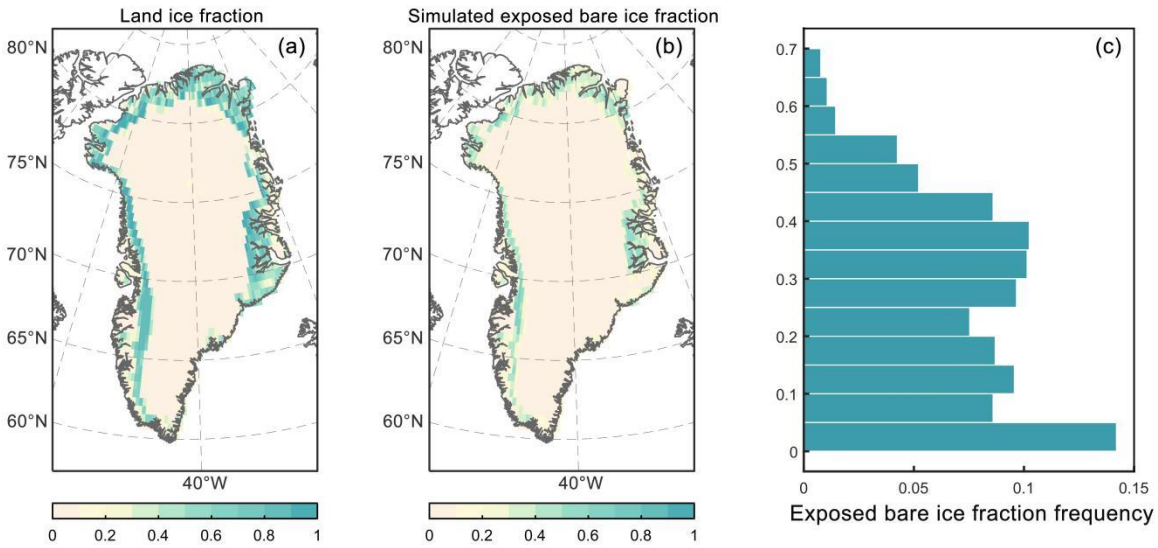

391

392 **Figure 6.** Spatial distribution of (a) the fraction of land ice underlying snowpack and (b)
393 exposed bare ice considering the snow cover simulated by CoLM SNICAR-ADv4 for the JJA
394 from 2000 to 2020. (c) Frequency distribution of exposed bare ice within the bare ice region
395 (excluding grid cells with no exposed bare ice), calculated as the proportion of grid cells
396 within each bare ice fraction interval relative to the total number of bare ice grid cells.

397

398 To assess whether the integration of an ice radiative transfer solver in CoLM improves albedo
399 simulations, we compared simulated albedo with the MCD43C3 albedo in shortwave, visible
400 and NIR regions of the spectrum during the summer of 2000-2020 in bare ice region (Fig. 7).
401 Both schemes of SNICAR-AD and SNICAR-ADv4 maintain consistent settings for default
402 snow albedo scheme, with sphere snow grain shape, adding-doubling radiative transfer solver,
403 and BC/dust-snow external mixing state. In other words, the differences in albedo simulated
404 by these two schemes are determined by the treatment for ice albedo. As seen in Figs. 7d-f, it
405 is obvious that the SNICAR-AD enabled CoLM albedo is significantly overestimated across
406 all bare ice region, by 0.086 in shortwave, 0.078 in visible and 0.095 in NIR. Compared with
407 CoLM SNICAR-AD, the application of the SNICAR-ADv4 scheme reduced the
408 overestimation of albedo for all bands, by 38% in the shortwave, 50% in the visible and 28%
409 in the NIR (Figs. 7d-i). Furthermore, comparative analysis of the spatial distributions of
410 correlation coefficients, root mean square errors (RMSE), and linear trends (Figs. S1-S3)
411 reveals that CoLM-SNICAR-ADv4 outperforms CoLM-SNICAR-AD across all evaluation

删除[o_0]:

删除[o_0]: **5**

删除[o_0]: Figure

删除[o_0]: 6

删除[o_0]: Figure

删除[o_0]: 6

删除[o_0]: 0.132

删除[o_0]: 0.131

删除[o_0]: 0.132

删除[o_0]: 60

删除[o_0]: 70

删除[o_0]: 48

删除[o_0]: Figure

删除[o_0]: 6

412 metrics. These metrics were derived from each grid cell by comparing the 21-year summer
413 albedo time series (2000-2020) from model simulations and MODIS observations: correlation
414 coefficients assess temporal agreement, RMSE quantifies deviation magnitudes, and linear
415 trends (obtained via least-squares regression) capture interannual albedo changes. The
416 comprehensive spatial evaluation demonstrates consistent improvements in both the spatial
417 pattern and quantitative representation.

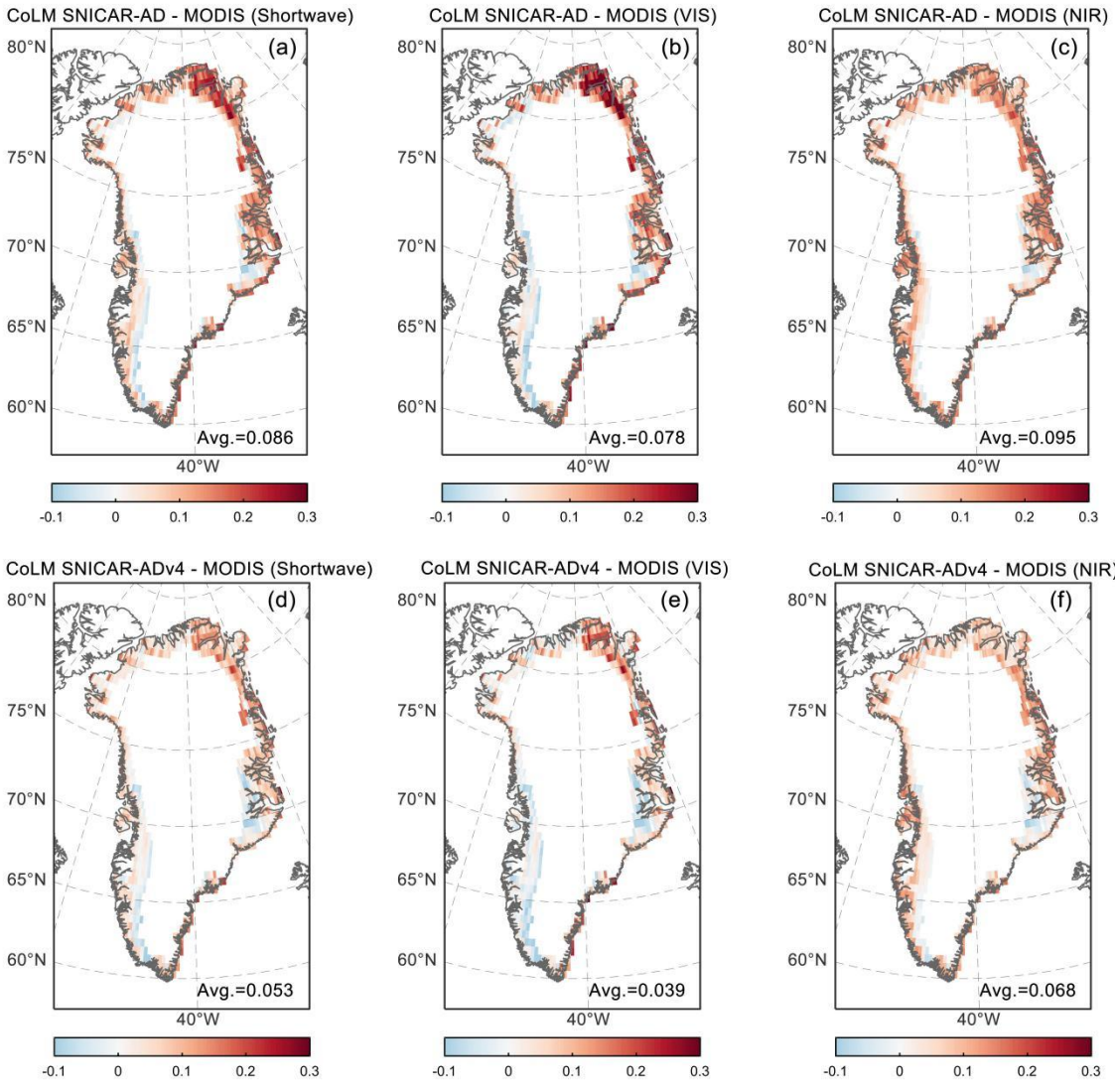

418

419 **Figure 7.** Spatial distribution of the difference of the 2000-2020 JJA albedo between the
420 CoLM with different snow/ice albedo schemes (SNICAR-AD and SNICAR-ADv4) and the
421 MCD43C3 in the (a, d) shortwave (0.3–5.0 μm), (b, e) visible (0.3–0.7 μm) and (c, f)
422 near-infrared (0.7–5.0 μm) bands.

423

删除[o_0]:

设置格式[o_0]: 两端对齐

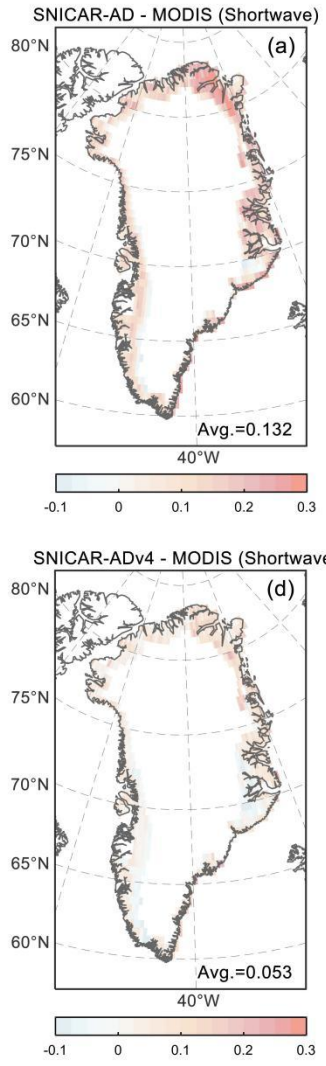

删除[o_0]:

删除[o_0]: **6**

The decrease in the positive bias of CoLM SNICAR-ADv4 can also be clearly seen in the shortwave, visible and near-infrared albedo time series, with the area-weighted mean albedo of the GrIS bare ice regions steadily decreasing throughout the summer period from 2000 to 2020, compared with CoLM SNICAR-AD (Fig. 8). The albedo of CoLM SNICAR-ADv4 fluctuates around 0.47 in the shortwave, 0.53 in the visible, and 0.4 in the NIR, which is approximately 0.05 higher than the corresponding values in MCD43C3. In addition, the CoLM SNICAR-ADv4 simulations exhibit synchronous variations in albedo with those of MCD43C3, and there are relatively high temporal correlations between the CoLM SNICAR-ADv4 and MCD43C4 albedo, with the values up to 0.95 for the shortwave, visible, and NIR bands. In contrast, the albedo from the CoLM SNICAR-AD shows lower correlation with MCD43C3 due to its constant ice albedo treatment. It is obvious that a large interannual variability in the SNICAR-ADv4 enabled CoLM albedo is in consistence with that of the MCD43C3, while the simulated albedo using SNICAR-AD scheme present a weaker interannual variability. Regarding correlation with observations, SNICAR-AD achieves slightly lower correlation (0.91) in the NIR band compared to its performance in the shortwave and visible bands (both 0.92).

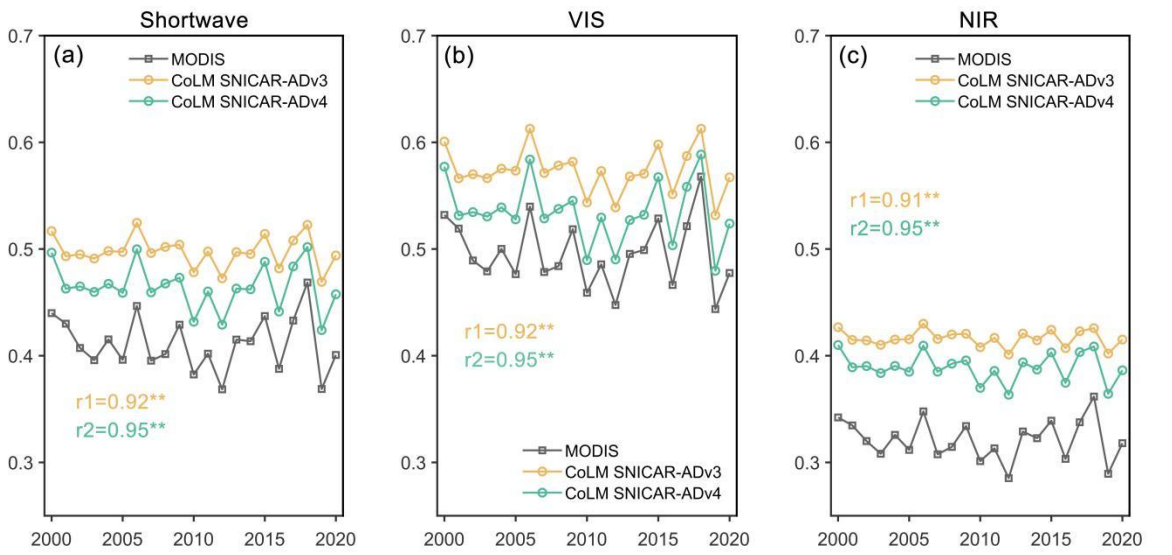

Figure 8. Time series of the 2000-2020 JJA CoLM SNICAR-AD and SNICAR-ADv4 albedo versus the MCD43C3 albedo over bare ice region, in the (a) shortwave (0.3–5.0 μm), (b) visible (0.3–0.7 μm) and (c) near-infrared (0.7–5.0 μm) bands. Double asterisks indicates significance at the 99% confidence level.

删除[o_0]: Temporally, the decrease in positive bias of CoLM SNICAR-ADv4 can be also clearly witnessed in the time series of shortwave, visible and NIR albedo, with the consistent lower area-weighted average albedo of GrIS bare ice region in all summertime from 2000 to 2020, by comparing it to that of CoLM SNICAR-AD

删除[o_0]: Figure

删除[o_0]: 7

删除[o_0]: SNICAR-ADv4 enabled simulations

删除[o_0]: 4

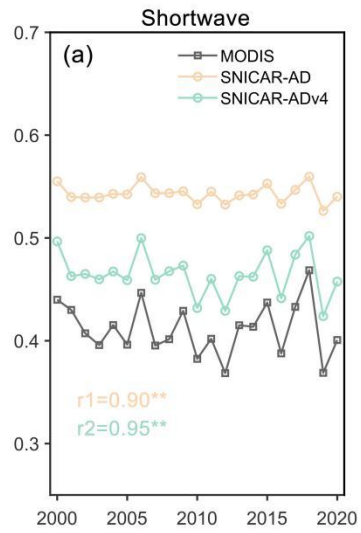

删除[o_0]:

删除[o_0]: 7

Given that the bias reduction varies across regions with different bare ice coverages, we explore the distribution of the albedo from CoLM SNICAR-AD, CoLM SNICAR-ADv4 and MCD43C3 under different bare ice fractions. Generally, as bare ice fraction increases, CoLM SNICAR-ADv4 can more effectively reduce the overestimation of shortwave broadband albedo (BBA) compared to CoLM SNICAR-AD, due to its improved simulation of bare ice BBA (Fig. 9). For regions where bare ice covers more than half the area, the albedo overestimation of SNICAR-AD was reduced significantly by up to 99%. When the bare ice fraction is between 0.4 and 0.5, the percentage of overestimation reduction in albedo decreases to 74%, followed by regions with bare ice fraction of 0.3-0.4 (52%), 0.2-0.3 (38%), 0.1-0.2 (25%), and 0-0.1 (10%), respectively.

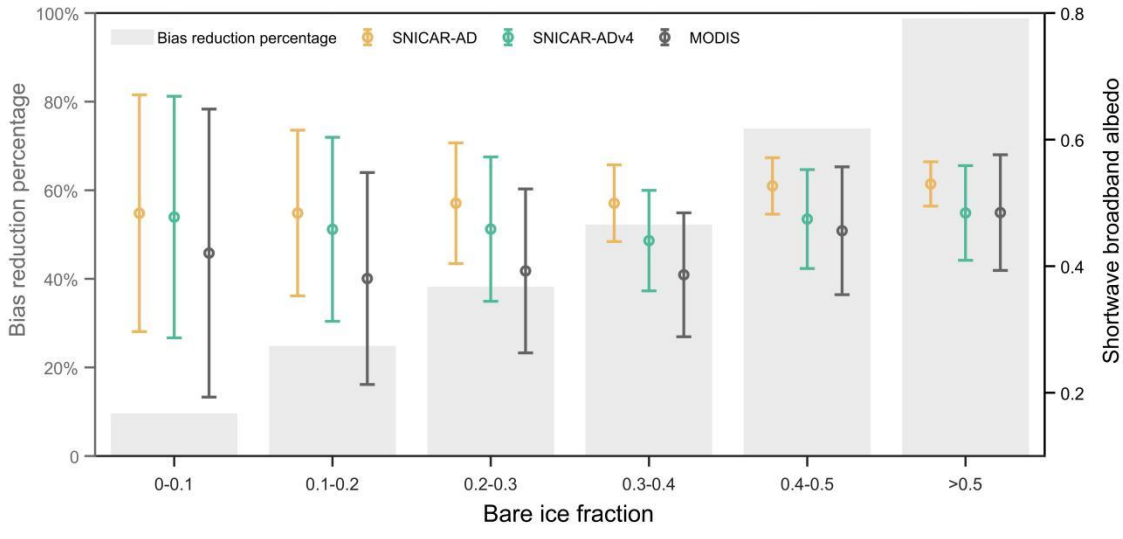

Figure 9. Mean shortwave broadband albedo from CoLM SNICAR-AD, CoLM SNICAR-ADv4 and MCD43C3 under different bare ice fractions (error plots). The uncertainty is calculated as double standard error, which reflects the 95% confidence interval. The percentages of CoLM SNICAR-ADv4 albedo reduction in bias are represented by grey bars.

删除[o_0]: Figure

删除[o_0]: 8

删除[o_0]: 88

删除[o_0]: 70

删除[o_0]: 57

删除[o_0]: 42

删除[o_0]: 20

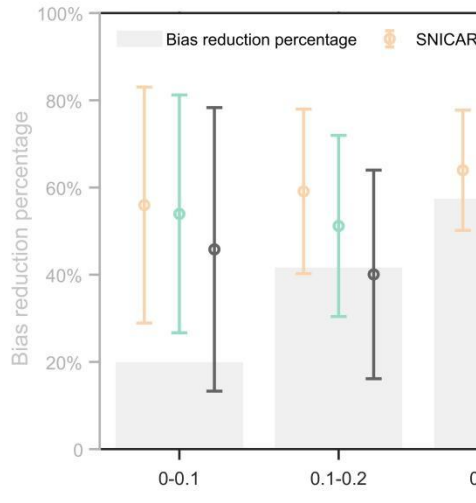

删除[o_0]:

删除[o_0]: **8**

3.3 A feedback revealed by bare ice properties change

The application of the SNICAR-ADv4 scheme in CoLM has significantly reduced the bias in albedo simulations. To investigate the regional climatic response to bare ice metamorphism of Greenland's bare ice region, we conduct a simulation in which the bare ice physical properties for each year are set to the values from 2000. By calculating the difference in simulated albedo between the simulations with annually varying bare ice properties and those using the 2000 values, the model sensitivities to the change in summer bare ice albedo can be assessed to quantify its impact on 2-m temperature and snow cover. To better highlight the impact of changes in bare ice physical properties, the study area was restricted to regions with a bare ice fraction larger than 0.4. Figures 10a-c compares the effects of bare ice metamorphism on the 21-year summer mean albedo, 2-m temperature and snow cover fraction, between simulations with annually varying bare ice properties and those using constant year-2000 properties. The regional weighted mean albedo difference between the two experiments reaches 0.032, indicating that the albedo in the bare ice region is reduced by 0.032 during the summer due to bare ice metamorphism (Fig. 10a). This leads to a 0.071°C 2-meter temperature forcing and a -0.011 change in snow cover fraction over the study period (Figs. 10b and c). These results suggest that the temperature increase associated with the change in albedo contributes to snow melting.

Spatially, the regions with strong response of near surface air temperature to bare ice albedo changes are concentrated in the edge of the northwestern and western ablation zone, where the 2-temperature increased by over 0.1°C in most part of these areas (Fig. 10b). A similar response pattern can be also seen in the difference distribution of the snow cover (Fig. 10c), with decrease in snow cover fraction exceeding 0.04 in parts of the northwestern and western GrIS where temperature increases are most pronounced. To further evaluate the hydrological implications of albedo-induced warming, we examined changes in snow water equivalent, which integrates snow accumulation, meltwater retention, and sublimation processes. This analysis indicates that bare ice metamorphism represented by annually varying ice properties leads to a forcing that causes an average snow water equivalent decrease of 1.345 mm (Fig.

删除[o_0]: significantly

删除[o_0]: Figure

删除[o_0]: 9

删除[o_0]: d

删除[o_0]: Figure

删除[o_0]: 9b

删除[o_0]: Figure

删除[o_0]: 9c

删除[o_0]: northeastern

删除[o_0]: .

10d), consistent with the observed snow cover decline. The statistical distributions of changes in 2-m temperature, snow cover, and snow water equivalent (Fig. 10e) reinforce the finding that certain regions of the GrIS are especially sensitive to reductions in bare ice albedo. These coordinated changes manifest a strong bare ice-albedo feedback in the GrIS bare ice region because bare ice albedo is reduced through physical and biological melt-albedo processes that darken the ice surface as the warming occurs in the ice surface.

The metamorphism of bare ice could be manifested in the changes in the ice density and air bubble radius with the ice, and these two factors jointly determine the specific surface area (Eq.1) which have one-to-one relationship with the bare ice albedo (Fig. 3b). From Fig. 10f, the difference in BBA shows a strong positive correlation with the specific surface area, with a correlation coefficient of 0.88 (significant at the 99% confidence level), since the two simulations differ solely in their bare ice physical property inputs to the land surface model. As more intense melt processes start in the early summer of the GrIS ablation zone after 2000, the lower specific surface area, linked with the bare ice-albedo feedback, consistently contributes to the reduction of the BBA (Fig. 10f). Additionally, according to the sensitivity of modeled spectral albedo to the relevant parameters of the standalone SNICAR-ADv4 model (Fig. 5), the decreased bare ice albedo, associated with a lower specific surface area, suggests an overall increase in ice density and a larger size of air bubbles within the ice in the GrIS bare ice region.

删除[o_0]: Such response of the temperature and snow cover

删除[o_0]: Figure

删除[o_0]: 2a

删除[o_0]: Figure

删除[o_0]: 9

删除[o_0]: d

删除[o_0]: since the control experiment only altered the bare ice physical property data input into the land surface model

删除[o_0]: commence

删除[o_0]: Figure

删除[o_0]: 9d

删除[o_0]: offline

删除[o_0]: Figure

删除[o_0]: 4

删除[o_0]:

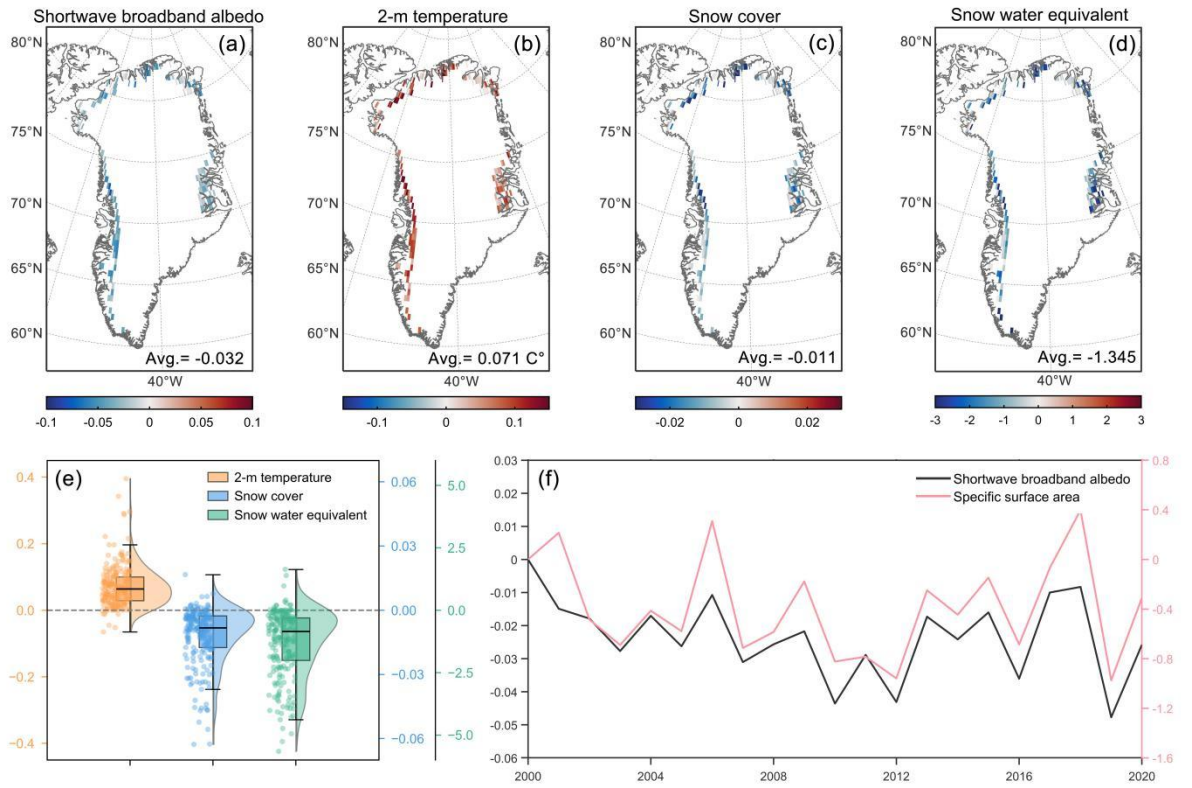

513

514 **Figure 10.** Spatial differences between simulations using annually varying bare ice properties
515 and those using fixed year-2000 values during JJA (June–August) from 2000 to 2020: (a)
516 surface albedo, (b) 2-m air temperature (°C), (c) snow cover fraction, and (d) snow water
517 equivalent. (e) Statistical distributions of differences in 2-m air temperature, snow cover, and
518 snow water equivalent, shown using combined boxplots, left-side jittered points, and
519 right-side half-violin plots. (f) Time series of differences in specific surface area ($m^2 \cdot kg^{-1}$)
520 and simulated shortwave broadband albedo between the two experiments.

521

522 After 2000, the metamorphism of bare ice in the Greenland bare ice region is mainly reflected
523 in the decrease of SSA, which leads to ice darkening. This, in turn, induces regional
524 near-surface temperature increases, causing snowmelt and ultimately resulting in a reduction
525 of snow cover. Changes in snow cover directly determine the extent of bare ice exposure and
526 significantly affect the albedo through snow-albedo feedback. The obvious snow cover
527 contraction attributed to the changes in the physical properties of bare ice will cause more
528 dark ice exposure and darkening, and make a constant contribution to albedo reduction in this
529 ablation zone, suggesting a potential linkage between the bare ice-albedo and the

设置格式[o_0]: 字体颜色: 背景 2

设置格式[o_0]: 字体颜色: 背景 2

删除[o_0]: region

删除[o_0]: effect

snow-albedo feedback.

4. Conclusions and Discussion

In this study, we incorporated SNICAR-ADv4 into the CoLM and made an enhanced MODIS-informed bare ice physical properties to explore the response of the bare ice albedo to the ice metamorphism under polar warming. The use of SNICAR-ADv4 in CoLM significantly reduces the severe overestimation originated from the default ice albedo treatment, with the improvement of the albedo modeling by 38%, 50% and 28% for the BBA, visible and NIR albedo. The snow and ice treatment used in CoLM SNICAR-ADv4 schemes, and SNICAR-AD are summarized in the Fig. 1, and it is evident that SNICAR-ADv4 performs radiative transfer calculations not only over the snow column but also over the ice column. During the summertime of 2000-2020, the bare ice BBA decreased by 0.032 due to the changes in bare ice physical properties. The subsequent darkening of the bare ice led to a 2-m air temperature forcing of 0.071°C, a change in snow cover of -0.011 and snow water equivalent of -1.345 mm over the 21-year period, suggesting that even a slight reduction in bare ice albedo can produce noticeable climate responses in ablation region.

Our results are consistent with, and extend, recent progress in modeling bare ice albedo modeling over the GrIS. Antwerpen et al. (2022) demonstrated that the regional MAR model overestimated bare ice albedo by 22.8% below 70°N, leading to significant underestimation of meltwater production. Similarly, Wicker-Clarke et al. (2024) found that the global ELM-E3SM model overestimated shortwave broadband albedo by ~5% due to the use of fixed albedo parameters, and showed that incorporating more realistic bare ice albedo reduced the surface mass balance by approximately 145 Gt between 2000 and 2021. Although both studies focus on the GrIS, they differ in model structure and spatial resolution: MAR is a high-resolution regional climate model, while ELM-E3SM is part of a coarser-resolution global Earth system model. Despite these differences, both studies highlight a persistent bias—systematic overestimation of bare ice albedo. The convergence of evidence from diverse modeling frameworks underscores the need to improve bare ice

删除[o_0]: 60
删除[o_0]: 70
删除[o_0]: 48
删除[o_0]: Figure
删除[o_0]: 10
删除[o_0]: 2021
删除[o_0]: and

representation in land surface models. Building on these insights, our study examines the role of bare ice metamorphism, particularly changes in specific surface area, in driving progressive surface darkening. By isolating the feedback between evolving ice properties and surface energy balance, we propose a physically mechanism for the observed albedo decline. Our sensitivity analysis underscores how bare ice metamorphism can influence surface energy balance and the importance of incorporating such processes in future model developments.

Our findings also highlight the role of the bare ice-albedo feedback linked to changes in ice surface properties, as shown in Fig. 11. A marked reduction in snow cover occurred due to lowered albedo in the ablation zone, exposing more bare ice and further reducing regional albedo, especially in northern GrIS. This agrees with previous findings that increased bare ice exposure has intensified the snow-albedo feedback in this region, with its strength rising by 51% from 2001 to 2017 (Ryan et al., 2019). The physical processes governing snowpack evolution play a crucial role in modulating surface albedo and associated feedbacks, particularly in the ablation zone of the GrIS, where snow loss accelerates bare ice exposure and amplifies radiative forcing. More specifically, new snow quickly loses reflectivity through grain growth and vapor diffusion, with subsequent changes driven by temperature gradients and compaction (Flanner and Zender, 2006). Meltwater accelerates these processes through melt-refreeze cycles (Brun 1989), creating a self-reinforcing system where both ice exposure and snow aging enhance surface darkening. While biological and hydrological factors such as algal growth play a secondary role in ice darkening (Ryan et al., 2019), our results demonstrate that changes in bare ice properties, particularly a downward trend in specific surface area at a rate of -0.007 yr^{-1}, exert significant control over meltwater production. We collectively term these processes of the variation in the bare ice albedo associated with snow melting the bare ice-snow-albedo feedback (Fig. 11). As rising temperatures may further reduce ice albedo, this feedback could substantially increase Greenland's contribution to sea level rise through enhanced melting (Ryan et al., 2019), highlighting the need for improved process understanding in climate projections.

This study advances our understanding of the performances of the GrIS's snow and ice albedo simulations using different snow/ice schemes (SNICAR-AD and SNCIAR-ADv4), and the amplifying effect of bare ice on the albedo reduction through bare ice-snow-feedback mechanism. However, three key limitations constrain our current findings. First, the 0.5°×0.5° resolution is insufficient to accurately represent the narrow ablation zone, and big resolution gap between MODIS data and the model output is a limitation of this study. Second, CoLM's representation of GrIS glaciers prescribed fixed ice thickness and mass with internally retained meltwater prevents calculation of surface mass balance, and excludes ice melt contributions to runoff. Although computationally efficient, this simplification systematically underestimates meltwater export from Greenland's ablation zones, where ice dynamical processes dominate mass loss. Third, methodological constraints prevent independent quantification of ice density and air bubble size effects, as their relationship is prescribed in the lookup table (ρ_{ice}=650 kg·m^{-3} corresponds to R_{eff}=100 μm, ρ_{ice}=916 kg·m^{-3} corresponds to R_{eff}=1500 μm) based on the standalone SNICAR-ADv4 model. Future work will address these limitations by employing higher-resolution modeling for more precise delineation of bare ice margins, coupling a dynamic ice sheet model to properly simulate the SMB and ice-melt runoff contributions, and establishing observational constraints on ice density and air bubble effective radius evolution to improve ice albedo modeling. Future efforts are also needed to consider the actual LACs concentrations within the ice, including BC, dust and snow algae, rather than relying on equivalent BC, and evaluate their impacts on GrIS mass loss using fully coupled land-atmosphere models, which may reveal more pronounced feedbacks than offline simulations.

设置格式[o_0]: 字体颜色: 背景 2

设置格式[o_0]: 字体颜色: 背景 2

设置格式[o_0]: 字体颜色: 背景 2

设置格式[o_0]: 字体颜色: 背景 2

删除[o_0]: In future research, we will study the effects of bare ice albedo changes at a higher resolution to accurately delineate bare ice regions.

删除[o_0]:

删除[o_0]: Besides, the current methods are still unable to distinguish how the ice density and the size of air bubbles change individually, as the relationship between ice density and the effective radius of air bubbles is arbitrarily prescribed (ρ_{ice}=650 kg.m^{-3} corresponds to R_{eff}=100 μm, ρ_{ice}=916 kg.m^{-3} corresponds to R_{eff}=1500 μm) when constructing the lookup table based on the offline SNICAR-ADv4 model. The precise inversion of ice density and the effective radius of air bubbles within the ice is a scientific problem worthy of further investigation.

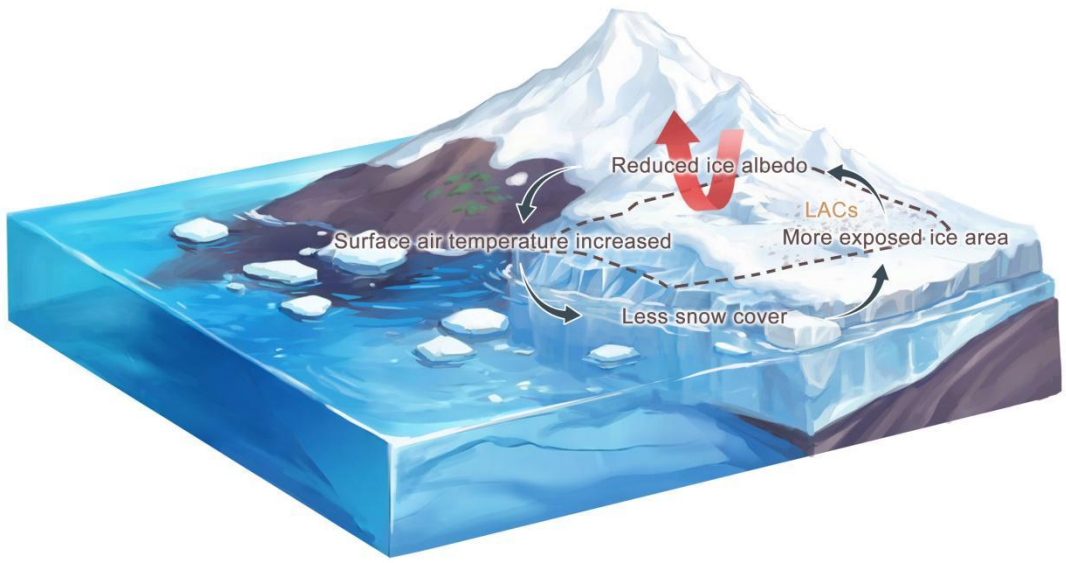

612

613 **Figure 11.** Illustration of the bare ice-snow-albedo feedback over the Greenland Ice Sheet. A
614 reduction in ice albedo, primarily driven by changes in bare ice surface properties, exposes
615 more bare ice, further lowering regional albedo and raising surface air temperatures. This
616 leads to a decline in snow cover, which accelerates bare ice exposure and reinforces radiative
617 forcing. This positive feedback loop intensifies melt, particularly in the ablation zone,
618 contributing to increased surface darkening and meltwater production.

619

620 *Data availability*. The SNICAR-ADv4 enabled CoLM2024 code is available on GitHub at
621 https://github.com/guoshuyang23/CoLM-SNICARADv4. The standalone SNICAR-ADv4
622 used in this study can be downloaded at https://github.com/chloewhicker/SNICAR-ADv4.
623 MODIS snow cover data (MOD10C1) used to make the cloud and snow mask for bare ice
624 pixels is available at https://nsidc.org/data/mod10c1/versions/6. MODIS surface reflectance
625 data (MOD09CMG) used to retrieve the bare ice properties is from
626 https://doi.org/10.5067/MODIS/MOD09CMG.061. MODIS surface albedo data (MCD43C3)
627 used to evaluate the simulations and retrieve the bare ice properties is from
628 https://doi.org/10.5067/MODIS/MCD43C3.061

629

630 *Author contributions*. SYG designed the study and wrote the paper. YJD was responsible for
631 to conceptualization, supervision, and funding acquisition. HY contributed to revisions of the

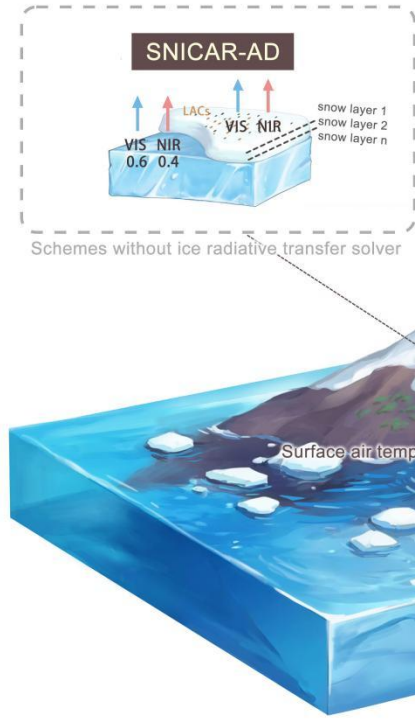

删除[o_0]:

删除[o_0]: **10**

设置格式[o_0]: 字体: 非加粗

设置格式[o_0]: 字体: 非加粗

设置格式[o_0]: 字体: 非加粗

删除[o_0]: offline

manuscript. HBL provided technical support.

Competing interests. The contact author has declared that neither they nor their co-authors have any competing interests.

Acknowledgements. We thank Chloe A. Whicker-Clarke for sharing the method for processing ice optical property files in the standalone SNICAR-ADv4 for use in land surface models.

Financial support. This research was funded by the Guangdong Major Project of Basic and Applied Basic Research (2021B0301030007), the Natural Science Foundation of China (under Grants U2342227, 42075160, and 42088101), the Southern Marine Science and Engineering Guangdong Laboratory (Zhuhai) (No. SML2023SP216), and the specific research fund of the Innovation Platform for Academicians of Hainan Province (YSPTZX202143).

删除[o_0]: Whicker

删除[o_0]: offline

设置格式[o_0]: 正文，行距: 单倍行距

References

Abolafia-Rosenzweig, R., He, C., McKenzie Skiles, S., Chen, F., and Gochis, D.: Evaluation and optimization of snow albedo scheme in Noah-MP land surface model using in situ spectral observations in the Colorado Rockies, J. Adv. Model. Earth Syst., 14, e2022MS003141, https://doi. org/10.1029/2022MS003141, 2022.

Alexander, P. M., Tedesco, M., Fettweis, X., van de Wal, R. S. W., Smeets, C. J. P. P., and van den Broeke, M. R.: Assessing spatio-temporal variability and trends in modelled and measured Greenland ice sheet albedo (2000–2013), The Cryosphere, 8(6), 2293–2312, https://doi.org/10. 5194/tc-8-2293-2014, 2014.

Antwerpen, R., Tedesco, M., Fettweis, X., Alexander, P.,and vandeBerg, W. J.: Assessing bare-ice albedo simulated byMAR overthe Greenland icesheet(2000–2021) andimplications formeltwater production estimates, The Cryosphere, 16(10), 4185–4199, https://doi.org/10. 5194/tc-16-4185-2022, 2022.

Box, J. E., Fettweis, X., Stroeve, J. C., Tedesco, M., Hall, D. K., and Steffen, K.: Greenland ice sheet albedo feedback: Thermodynamics and atmospheric drivers, The Cryosphere, 6(4), 821–839, https://doi.org/10.5194/tc-6-821-2012, 2012.

Briegleb, B. P. and Light, B.: A Delta-Eddington multiple scattering parameterization for solar radiation in the sea ice component of the Community Climate System Model, NCAR/TN472+STR, National Center for Atmospheric Research, 108 pp., https://doi.org/10.5065/D6B27S71, 2007.

Brun, E.: Investigation of wet-snow metamorphism in respect of liquid-water content, Ann. Glaciol., 13, 22 – 26, https://doi.org/10.3189/S0260305500007635, 1989.

Chen, X., Zhang, X. , Church, J. A., Watson, C. S., King, M. A., Monselesan, D., Legresy, B., and Harig C.: The increasing rate of global mean sea-level rise during 1993-2014, Nat. Clim. Change,7, 492–495, https://doi.org/10.1038/nclimate3325, 2017.

Chevrollier, L. A., Cook, J. M., Halbach, L., Jakobsen, H., Benning, L. G., Anesio, A. M., and Tranter, M.: Light absorption and albedo reduction by pigmented microalgae on

675 snow and ice, J. Glaciol., 69(274), 333–341. https://doi.org/10.1017/jog.2022.64, 2023.

676 Cogley, J. G., Hock, R., Rasmussen, L. A., Arendt, A. A., Bauder, A., Braithwaite, R. J.,
677 Jansson, P., Kaser, G., Möller, M., Nicholson, L.: Glossary of glacier mass balance and
678 related terms (p. 86), IHP-VII Technical Documents in Hydrology No, 2011.

679 Cook, J. M., Tedstone, A. J., Williamson, C., McCutcheon, J., Hodson, A. J., Dayal, A.,
680 Skiles, M., Hofer, S., Bryant, R., McAree, O., McGonigle, A., Ryan, J., Anesio, A. M.,
681 Irvine-Fynn, T. D. L., Hubbard, A., Hanna, E., Flanner, M., Mayanna, S., Benning, L. G.,
682 van As, D., Yallop, M., McQuaid, J. B., Gribbin, T., and Tranter, M.: Glacier algae
683 accelerate melt rates on the south-western Greenland Ice Sheet, The Cryosphere, 14,
684 309330, https://doi.org/10.5194/tc-14-309-2020, 2020.

685 Danabasoglu, G., Lamarque, J. F., Bacmeister, J., Bailey, D. A., DuVivier, A. K., Edwards, J.,
686 Emmons, L. K., Fasullo, J. T., Garcia, R., Gettelman, A., Hannay, C., Holland, M. M.,
687 Large, W. G., Lauritzen, P., Lawrence, D. M., Lenaerts-Jan T. M., Lindsay, K.,
688 Lipscomb, W. H, Mills, M. J., Neale, R., Oleson, K., Otto-Bliesner, B., Phillips, A. S.,
689 Sacks, W. J., Tilmes, S., van Kampenhout, L., Vertenstein, M., Bertini, A., Dennis, J.,
690 Deser, C., Fischer, C., Fox-Kemper, B., Elizabeth-Kay, J., Kinnison, D., Kushner, P.,
691 Larson, V. E., Long, M., Mickelson, S., Moore, J. K., Nienhouse, E., Polvani, L., Rasch,
692 P. J., and Strand, W. G..: The community Earth system model version 2 (CESM2), J.
693 Adv. Model. Earth Syst., 12, https://doi.org/10.1029/2019MS001916, 2020.

694 Dang, C., Zender, C. S., and Flanner, M. G.: Intercomparison and improvement of
695 two-stream shortwave radiative transfer schemes in Earth system models for a unified
696 treatment of cryospheric surfaces, The Cryosphere, 13(9), 2325–2343.
697 https://doi.org/10.5194/tc-13-2325-2019, 2019.

698 Feng, S., Cook, J. M., Naegeli, K., Anesio, A. M., Benning, L. G., and Tranter, M.: The
699 impact of bare ice duration and geo-topographical factors on the darkening of the
700 Greenland Ice Sheet, Geophys. Res. Lett., 51, e2023GL104894, https://doi.
701 org/10.1029/2023GL104894, 2024.

702 Flanner, M. G., and Zender, C. S. Linking snowpack microphysics and albedo evolution, J.

删除[o_0]: Dickinson, R. E., Henderson-Sellers, A., and Kennedy, P. J.: Biosphere-atmosphere transfer scheme (BATS) for the NCAR community climate model (NCAR Tech. Note NCAR/TN-38+STR, Vol. 82), National Center for Atmospheric Research, 1986

Geophys. Res., 111(D12), https://doi.org/10.1029/2005JD006834, 2006.

Flanner, M. G., Arnheim, J. B., Cook, J. M., Dang, C., He, C., Huang, X., Singh, D., Skiles, S. M., Whicker, C. A., and Zender, C. S.: SNICAR-ADv3: a community tool for modeling spectral snow albedo, Geosci. Model Dev., 14, 7673 – 7704, https://doi.org/10.5194/gmd-14-7673-2021, 2021.

Flanner, M. G., Liu, X., Zhou, C., Penner, J. E., and Jiao, C.: Enhanced solar energy absorption by internally-mixed black carbon in snow grains, Atmos. Chem. Phys., 12(10), 4699–4721, https://doi.org/10.5194/acp-12-4699-2012, 2012.

Flanner, M. G., Zender, C. S., Randerson, J. T., and Rasch, P. J.: Present-day climate forcing and response from black carbon in snow. J. Geophys. Res., 112(D11). https://doi.org/10.1029/2006jd008003, 2007.

Friedl, M.A., Sulla-Menashe, D., Tan, B., Schneider, A., Ramankutty, N., Sibley, A., and Huang X.: Modis collection 5 global land cover: algorithm refinements and characterization of new datasets. Remote Sens. Environ, 114(1), 168–182, https://doi.org/10.1016/j.rse.2009.08.016, 2010

Gardner, A. S., and Sharp, M. J.: A review of snow and ice albedo and the development of a new physically based broadband albedo parameterization, J. Geophys. Res., 115(F1), F01009, https://doi.org/10.1029/2009JF001444, 2010.

Hao, D., Bisht, G., Rittger, K., Bair, E., He, C., Huang, H., Dang, C., Stillinger, T., Gu., Y., Wang, H., Qian, Y., Leung, L. R.: Improving snow albedo modeling in the E3SM land model (version 2.0) and assessing its impacts on snow and surface fluxes over the Tibetan Plateau, Geosci. Model Dev., 16(1), 75–94, https://doi.org/10.5194/gmd-16-75-2023, 2023.

He, C., and Flanner, M.: Snow albedo and radiative transfer: Theory, modeling, and parameterization. In Springer series in light scattering (pp. 67–133), Springer, 2020.

He, C., Flanner, M. G., Chen, F., Bariage, M., Liou, K. N., Kang, S., Ming, J., and Qian, Y.: Black carbon-induced snow albedo reduction over the Tibetan Plateau: Uncertainties

from snow grain shape and aerosol–snow mixing state based on an updated SNICAR model, Atmos. Chem. Phys., 18, 11507–11527, https://doi.org/10.5194/ACP-18-11507-2018, 2018.

He, C., Flanner, M., Lawrence, D. M., and Gu, Y.: New features and enhancements in community land model (CLM5) snow albedo modeling: Description, sensitivity, and evaluation, J. Adv. Model. Earth Syst., 16, e2023MS003861, https://doi. org/10.1029/2023MS003861, 2024.

He, C., Liou, K. N., Takano, Y., Chen, F., and Barlage, M.: Enhanced snow absorption and albedo reduction by dust-snow internal mixing: Modeling and parameterization, J. Adv. Model. Earth Syst., 11(11), 3755–3776, https://doi.org/10.1029/2019ms001737, 2019.

He, C., Takano, Y., Liou, K. N., Yang, P., Li, Q., and Chen, F.: Impact of snow grain shape and black carbon–snow internal mixing on snow optical properties: Parameterizations for climate models, Journal of Climate, 30(24), 10019–10036, https://doi.org/10.1175/jcli-d-17-0300.1, 2017.

Hofer, S., Tedstone, A. J., Fettweis, X. and Bamber, J. L.: Decreasing cloud cover drives the recent mass loss on the Greenland Ice Sheet, Sci. Adv., 3, e1700584, https://doi.org/10.1126/sciadv.1700584, 2017.

King, M. D., Howat, I. M., Candela, S. G., Noh, M. J., Jeong, S., Noël, B. P. Y., Van den Broeke, M. R., Wouters, B., and Negrete, A.: Dynamic ice loss from the Greenland Ice Sheet driven by sustained glacier retreat, Commun. Earth Environ., 1(1), 1. https://doi.org/10.1038/s43247-020-0001-2, 2020.

Kochtitzky, W., Copland, L., King, M., Hugonnet, R., Jiskoot, H., Morlighem, M., Millan, R., Khan, S. A., and Noël, B.: Closing Greenland's mass balance: Frontal ablation of every Greenlandic glacier from 2000 to 2020, Geophys. Res. Lett., 50, e2023GL104095, https://doi. org/10.1029/2023GL104095, 2023.

Li, Y., Yang, K., Gao, S., Smith, L.C., Fettweis, X., and Li, M.: Surface meltwater runoff routing through a coupled supraglacial-proglacial drainage system, Inglefield Land, northwest Greenland, Int. J. Appl. Earth. Obs, Geoinf, p. 106.

https://doi.org/10.1016/j.jprocont.2022.08.003, 2022.

Mouginot, J., Rignot, E., Bjørk, A. A., van den Broeke, M., Millan, R., Morlighem, M., Noël, B., Scheuchl, B., and Wood, M.: Forty-six years of Greenland Ice Sheet mass balance from 1972 to 2018, P. Natl. Acad. Sci., 116, 9239–9244, https://doi.org/10.1073/pnas.1904242116, 2019.

Mullen, P. C., and Warren, S. G.:. Theory of the optical properties of lake ice, J. Geophys. Res., 93(D7), 8403–8414, https:// doi.org/10.1029/JD093iD07p08403, 1988.

Naegeli, K., Damm, A., Huss, M., Wulf, H., Schaepman, M., and Hoelzle, M.: Cross-Comparison of albedo products for glacier surfaces derived from airborne and satellite (Sentinel-2 and Landsat 8) optical data, Remote Sens., 9(2), 110. https://doi.org/10.3390/ rs9020110, 2017.

Nolin, A.W., and Stroeve, J.: The changing albedo of the Greenland ice sheet: implications for climate modeling, Ann. Glaciol., 25, 51–57. https://doi. org/10.1017/s0260305500013793, 1997.

Picard, G., Libois, Q., and Arnaud, L.: Refinement of the ice ab-sorption spectrum in the visible using radiance profile measurements in Antarctic snow, The Cryosphere, 10(6), 2655–2672, https://doi.org/10.5194/tc-10-2655-2016, 2016

Ryan, J. C.: Contribution of surface and cloud radiative feedbacks to Greenland Ice Sheet meltwater production during 2002-2023, Commun. Earth Environ., 5(538), https://doi.org/10.1038/s43247-024-01714-y, 2024.

Ryan, J. C., Smith, L. C., van As, D., Cooley, S. W., Cooper, M. G., Pitcher, L. H., and Hubbard, A.: Greenland Ice Sheet surface melt amplified by snowline migration and bare ice exposure, Sci. Adv., 5(3), eaav3738, https://doi.org/10.1126/sciadv.aav3738, 2019.

Sasgen, I., Wouters, B., Gardner, A.S., King, M.D., Tedesco, M., Landerer, F.W., Dahle, C., Save, H., and Fettweis, X.: Return to rapid ice loss in Greenland and record loss in 2019 detected by the GRACE-FO satellites, Commun. Earth Environ, 1, 1-8.

https://doi.org/10.1038/s43247-020-0010-1, 2020.

Schaaf, C., Wang, Z., and Strahler, A. H.: Commentary on Wang and Zender-MODIS snow albedo bias at high solar zenith angles relative to theory and to in situ observations in Greenland, Remote. Sens. Environ., 115, 1296 − 1300, https://doi.org/10.1016/j.rse.2011.01.002, 2011.

Schaaf, C., and Wang, Z.: MODIS/Terra+Aqua BRDF/Albedo Albedo Daily L3 Global 0.05Deg CMG V061 [Dataset]. NASA EOSDIS Land Processes DAAC, https://doi.org/10.5067/MODIS/MCD43C3.06, 2021.1

Schneider, A., Flanner, M., De Roo, R., and Adolph, A.: Monitoring of snow surface near-infrared bidirectional reflectance factors with added light-absorbing particles. The Cryosphere, 13(6), 1753–1766, https://doi.org/10.5194/tc-13-1753-2019, 2019

Schneider, A., Zender, C., Loeb, N., and Price, S.: Useofshallow icecoremeasurements toevaluate andconstrain 1980–1990 global reanalyses oficesheetprecipitation rates. Geophys. Res. Lett., 50(19), e2023GL103943, https://doi.org/10.1029/2023GL103943, 2023

Shimada, R., Takeuchi, N., and Aoki, T.: Inter-annual and geographical variations in the extent of bare ice and dark ice on the Greenland ice sheet derived from MODIS satellite images, Front Earth Sci., 4, 43, https://doi.org/10.3389/feart.2016.00043, 2016.

Stibal, M., Box, J. E., Cameron, K. A., Langen, P. L., Yallop, M. L., Mottram, R. H., Khan, A. L., Molotch, N. P., Chrismas, N. A. M., Quaglia, F. C., Remias, D., Smeets, P., Van den Broeke, M. R., and Ryan, J.: Algae drive enhanced darkening of bare ice on the Greenland ice sheet, Geophys. Res. Lett., 44(22), 11463–11471, https://doi.org/10.1002/2017GL075958, 2017.

Stroeve, J., Box, J. E., Gao, F., Liang, S., Nolin, A., and Schaaf, C.: Accuracy assessment of the MODIS 16-day albedo product for snow: Comparisons with Greenland in situ measurements, Remote. Sens. Environ., 94(1), 46–60. https://doi.org/10.1016/j.rse.2004.09.001, 2005.

812 Tedesco, M., Doherty, S., Fettweis, X., Alexander, P., Jeyaratnam, J., and Stroeve, J.: The
813 darkening of the Greenland ice sheet: Trends, drivers, and projections (1981–2100), The
814 Cryosphere, 10(2), 477–496, https://doi.org/10.5194/tc-10-477-2016, 2016.

815 Tedstone, A. J., Cook, J. M., Williamson, C. J., Hofer, S., McCutcheon, J., Irvine-Fynn, T.,
816 Gribbin, T., and Tranter, M.: Algal growth and weathering crust state drive variability in
817 western Greenland Ice Sheet ice albedo, The Cryosphere, 14, 521–538,
818 https://doi.org/10.5194/tc-14-521-2020, 2020.

819 Tedstone, A. J., Bamber, J. L., Cook, J. M., Williamson, C. J., Fettweis, X., Hodson, A. J.,
820 and Tranter, M.: Dark ice dynamics of the south-west Greenland Ice Sheet, The
821 Cryosphere, 11, 24912506, https://doi.org/10.5194/tc-11-2491-2017, 2017.

822 Toon, O. B., McKay, C. P., Ackerman, T. P., and Santhanam, K.: Rapid calculation of
823 radiative heating rates and photodissocia-tion rates in inhomogeneous multiple
824 scattering atmospheres, J. Geophys. Res., 94(D13), 16287–16301,
825 https://doi.org/10.1029/ jd094id13p16287, 1989.

826 Urraca, R., Lanconelli, C., and Cappucci, F.: Gobron, N. Comparison of Long-Term Albedo
827 Products against Spatially Representative Stations over Snow, Remote Sens., 14, 3745.
828 https://doi.org/ 10.3390/rs14153745, 2022.

829 van den Broeke, Box, J., Fettweis, X., Hanna, E., Noël, B., Tedesco, M., van As, D., van de
830 Berg, W. J., and van Kampenhout, L.: Greenland Ice Sheet Surface Mass Loss: Recent
831 Developments in Observation and Modeling, Curr. Clim. Change Rep., 3, 345356,
832 https://doi.org/10.1007/s40641-017-0084-8, 2017.

833 Vermote, E.: MODIS/Terra Surface Reflectance Daily L3 Global 0.05Deg CMG V061 [Data
834 set]. NASA EOSDIS Land Processes Distributed Active Archive Center,
835 https://doi.org/10.5067/MODIS/MOD09CMG.061. 2021.

836 Warren, S. G., and Wiscombe, W. J.:. A model for the spectral albedo of snow. II: Snow
837 containing atmospheric aerosols, J. Atmos. Sci., 37(12), 2734–2745,
838 https://doi.org/10.1175/1520-0469(1980)037<2734:amftsa>2.0.co;2, 1980.

Whicker-Clarke, A., Antwerpen, R., Flanner, M. G., Schneider, A., Tedesco, M., and Zender, C. S.: The effect of physically based ice radiative processes on Greenland ice sheet albedo and surface mass balance in E3SM, J. Geophys. Res.-Atmos., 129, e2023JD040241, https://doi.org/10.1029/ 2023JD040241, 2024.

Whicker-Clarke, A., Flanner, M. G., Dang, C., Zender, C. S., Cook, J. M., and Gardner, A. S.: SNICAR-ADv4: A physically based radiative transfer model to represent the spectral albedo of glacier ice, The Cryosphere, 16(4), 1197–1220, https://doi.org/10.5194/tc-16-1197-2022, 2022.

Williamson, C. J., Anesio, A. M., Cook, J., Tedstone, A., Poniecka, E., Holland, A., Fagan, D., Tranter, M., and Yallop, M.: Ice algal bloom development on the surface of the Greenland Ice Sheet, FEMS Microbiol. Ecol., 94(3), https://doi.org/10.1093/femsec/fiy025, 2018.

Wiscombe, W. J., and Warren, S. G.: A model for the spectral albedo of snow. I: Pure snow. J. Atmos. Sci., 37(12), 2712–2733. https://doi.org/10.1175/1520-0469(1980)037<2712:amftsa>2.0.co;2, 1980.

Ye, F., Cheng, Q., Hao, W., Yu, D., Ma, C., Liang, D., and Shen, H.: Reconstructing daily snow and ice albedo series for Greenland by coupling spatiotemporal and physics-informed models, Int. J. Appl. Earth Obs., 124, 103519, https://doi.org/10.1016/j.jag.2023.103519, 2023.

删除[o_0]: Whicker

删除[o_0]: C.

删除[o_0]: Whicker

删除[o_0]: C.